Feeding compact bulges and supermassive black holes with low angular-momentum cosmic gas at high redshift

Yohan Dubois[1,2]⋆, Christophe Pichon[1], Martin Haehnelt[3], Taysun Kimm[2], Adrianne Slyz[2], Julien Devriendt[2,4], and Dmitry Pogosyan[5]

[1] *Institut dAstrophysique de Paris, UMR 7095, CNRS, UPMC Univ. Paris VI, 98 bis boulevard Arago, 75014, Paris, France*
[2] *Sub-department of Astrophysics, University of Oxford, Keble Road, OX1 3RH, Oxford, UK.*
[3] *Institute of Astronomy and Kavli Institute for Cosmology, Madingley Road, CB3 0HA, Cambridge, United Kingdom.*
[4] *Observatoire de Lyon, UMR 5574, 9 avenue Charles André, F-69561, Saint Genis Laval, France.*
[5] *Department of Physics, University of Alberta, 11322-89 Avenue, Edmonton, T6G 2G7, Alberta, Canada.*

ABSTRACT

We use cosmological hydrodynamical simulations to show that a significant fraction of the gas in high redshift rare massive halos falls nearly radially to their very centre on extremely short timescales. This process results in the formation of very compact bulges with specific angular momentum a factor $5 - 30$ smaller than the average angular momentum of the baryons in the whole halo. Such low angular momentum originates both from segregation and effective cancellation when the gas flows to the centre of the halo along well defined cold filamentary streams. These filaments penetrate deep inside the halo and connect to the bulge from multiple rapidly changing directions. Structures falling in along the filaments (satellite galaxies) or formed by gravitational instabilities triggered by the inflow (star clusters) further reduce the angular momentum of the gas in the bulge. Finally, the fraction of gas radially falling to the centre appears to increase with the mass of the halo; we argue that this is most likely due to an enhanced cancellation of angular momentum in rarer halos which are fed by more isotropically distributed cold streams. Such an increasingly efficient funneling of low-angular momentum gas to the centre of very massive halos at high redshift may account for the rapid pace at which the most massive super massive black holes grow to reach observed masses around $10^9 \mathrm{M}_\odot$ at an epoch when the Universe is barely 1 Gyr old.

Key words: cosmology: theory — galaxies: evolution — galaxies: formation — galaxies: halos — galaxies: kinematics and dynamics — large-scale structure of Universe

1 INTRODUCTION

Supermassive black holes (BH) have been established to be ubiquitous at the centre of local galactic bulges and their mass has been shown to correlate well with the stellar mass and perhaps even more strongly with the stellar velocity dispersion of these bulges (Magorrian et al. 1998; Tremaine et al. 2002; Häring & Rix 2004). As the accretion of gas onto BHs can drive strong feedback from Active Galactic Nuclei (AGN) through spherical winds or collimated jets, and can potentially self-regulate the growth of the BH along with the cold baryon content of galaxies (Silk & Rees 1998; Haehnelt et al. 1998; King 2003) AGN feedback is a natural candidate to explain the observed cor-

relations. Indeed, this picture has been further substantiated by several numerical implementations of such feedback using either semi-analytical models (Bower et al. 2006; Croton et al. 2006; Somerville et al. 2008) or hydrodynamical simulations (Di Matteo et al. 2005; Booth & Schaye 2009; Dubois et al. 2012).

The issue is further complicated by the fact that the most supermassive BHs (several $10^9 \mathrm{M}_\odot$) seem to be already in place at $z \approx 6 - 7$, i.e. less than a Gyr after the Big-Bang (Willott et al. 2003; Fan et al. 2006; Jiang et al. 2009; Mortlock et al. 2011). Growth to such large masses in such a short time scale constitutes a significant challenge for any model of BH evolution, especially those with strong AGN feedback, as it requires sustained feeding at close to the Eddington accretion rate (Haiman 2004; Sijacki et al. 2009). However, considering that a substantial fraction of the sky

⋆ E-mail: dubois@iap.fr

had to be surveyed to discover the luminous QSOs powered by these very massive high-redshift BHs ($10^{-9}\,\mathrm{Mpc}^{-3}$ comoving number density of high-redshift quasars according to Fan et al. 2006), it appears likely that the halos hosting these BHs are the most massive formed at these early times and thus are very rare objects. Obviously, the main caveat of this 'rareness' argument is that since these young BHs are thought to be growing fast because of the presence of large amounts of gas in their surroundings, a larger number of their quasar counterparts could possibly be obscured in optical wavebands (Alexander et al. 2003; Treister et al. 2011; Willott 2011) and only be visible in X-rays (e.g. Daddi et al. 2007) and the Infrared. This selection effect could increase the *true* number of very bright quasars/super massive BHs at high redshift considerably.

Nevertheless, even when adopting the view that these objects are rare, one still needs to propose an effective mechanism to funnel low angular momentum gas all the way down to the sphere of influence of the BHs at the very centre of their very massive halos hosts. Hydrodynamical simulations suggest that high-redshift quasars are accreting gas at rates close to their Eddington (or super-Eddington) limit because large amounts of cold gas are indeed trapped in the centre of galaxies, and that the fraction of Eddington-limited growth of BHs diminishes with time as this gas reservoir is depleted (Sijacki et al. 2007; Di Matteo et al. 2008; Dubois et al. 2012). Di Matteo et al. (2012) have emphasized that filamentary infall of cold gas is the major mode of gas supply for the continuous feeding of BHs similar to what is discussed for the build-up of galaxies at intermediate redshift (Kereš et al. 2005; Agertz et al. 2009). Note that this is a very different mode of gas supply from that due to the often invoked more episodic feeding of BHs due to large amounts of gas driven to galactic nuclei by (major) mergers (Mihos & Hernquist 1996; Kauffmann & Haehnelt 2000; Hopkins et al. 2006; Mayer et al. 2010)

Pichon et al. (2011) and Kimm et al. (2011) have recently used hydro cosmological Adaptive Mesh Refinement (AMR) simulations to investigate the angular momentum properties and the infall of gas in Milky Way class halos at low and intermediate redshifts with a view to study the formation and evolution of their central galaxy discs. With a similar technique Bournaud et al. (2011) have performed simulations of isolated galaxy discs with parsec resolution to show that Toomre instabilities drive strong inflows of gas to the centre of these discs.

We build here on this work, by investigating the more massive and rarer halos expected to host the most massive supermassive BHs at high redshift. We therefore concentrate our exploratory study on the gas with the lowest angular momentum falling to the centre of these rare, massive halos.

Whilst Di Matteo et al. (2012) have recently investigated this problem using a simulation with a large enough volume ($533\,h^{-1}\cdot\mathrm{Mpc}$) to capture halos sufficiently massive to plausibly host these $\sim 10^9\,\mathrm{M}_\odot$ BHs, we take a different approach here and focus our study on two individual very massive halos at high redshift which we follow using a high-resolution cosmological hydrodynamics re-simulation technique. The main aim here is to better resolve the dynamics and angular momentum history of the inflowing cold gas as it falls to the centre of halos, forms a galactic bulge and potentially feeds the growth of the central supermassive BH.

The paper is organized as follows. Section 2 describes the numerical setup of our simulations. Section 3 investigates the angular momentum evolution and the typical trajectories of the baryonic material forming the bulge. Section 4 discusses the implications for BH build up at high redshift while Section 5 gives our conclusions.

2   THE NUMERICAL SIMULATIONS

We have performed two simulations with two different constrained initial conditions, generated using the `constrfield` package of `mpgrafic` (Prunet et al. 2008). The `constrfield` package generates realizations of the initial density field, subject to constraints (Bardeen et al. 1986; Hoffman & Ribak 1991) on the linear properties of an arbitrary set of spherical patches. A patch is defined by its position, size (or mass) and the window function. Any of the following patch properties, averaged over the window, can be specified as the constraints: the overdensity, the velocity, the velocity shear, the gradient of the density (set to zero if a patch represents the peak-patch progenitor of the collapsing halo) and the matrix of the second derivatives of the density that defines the initial ellipticity of the density profile in a patch. The `mpgrafic` realization of `constrfield` follows closely the code developed for Cosmic Web studies in Bond et al. (1996).

The first simulation was chosen to produce a halo with a Virial mass of $M_{\mathrm{vir}} = 2 \cdot 10^{15} M_\odot$ at $z = 0$ (which has a mass of $M_{\mathrm{vir}} = 5 \cdot 10^{11} M_\odot$ at $z = 6$) and the second a halo with a mass of $M_{\mathrm{vir}} = 2.5 \cdot 10^{12} M_\odot$ at $z = 6$. In the following, we will refer to the two simulation as SH and LH, respectively. For our chosen cosmological parameters (see below) the entire Universe should contain about $\sim 2 \cdot 10^4$ halos as massive as the one in the SH simulation while we should find only one halo as massive as the one in the LH simulation (but note that this depends very sensitively on the assumed matter power spectrum normalization). Our simulations should therefore represent a rare and a very rare massive halo respectively, and we refer to Table 1 for the basic properties of the two halos. Note that while the halo in the SH simulation has a fairly typical spin parameter of $\lambda = 0.05$ at $z = 6$ the halo in LH has a value twice higher, due to an ongoing merger. Such factor of two fluctuations of the spin parameter are not unusual during the build up of halos. To set up initial conditions, only the overdensity and peak (zero gradient) constraints were used with a top-hat window filtering that corresponds to the chosen masses. Overdensity values were selected to ensure that the halo collapses by the required redshift.

We assume a flat ΛCDM cosmology with total matter density $\Omega_m = 0.27$, baryon density $\Omega_b = 0.045$, dark energy density $\Omega_\Lambda = 0.73$, amplitude of the matter power spectrum $\sigma_8 = 0.8$ and Hubble constant $H_0 = 70\,\mathrm{km}\cdot\mathrm{s}^{-1}\cdot\mathrm{Mpc}^{-1}$ consistent with the WMAP 7-year data (Komatsu 2011). The box size of our simulations is $L_{\mathrm{box}} = 100\,h^{-1}\cdot\mathrm{Mpc}$ for both simulations. We generate high-resolution initial conditions within a small Lagrangian region enclosing all dark matter (DM) particles that end up within $2\,r_{\mathrm{vir}}$ of the halo at $z = 6$. The DM particles have a mass of $M_{\mathrm{res}} = 9 \cdot 10^5\,h^{-1}\cdot\mathrm{M}_\odot$ and $7 \cdot 10^6\,h^{-1}\cdot\mathrm{M}_\odot$ in the SH and LH simulation, respectively. That corresponds to an equivalent 4096^3 cartesian grid for
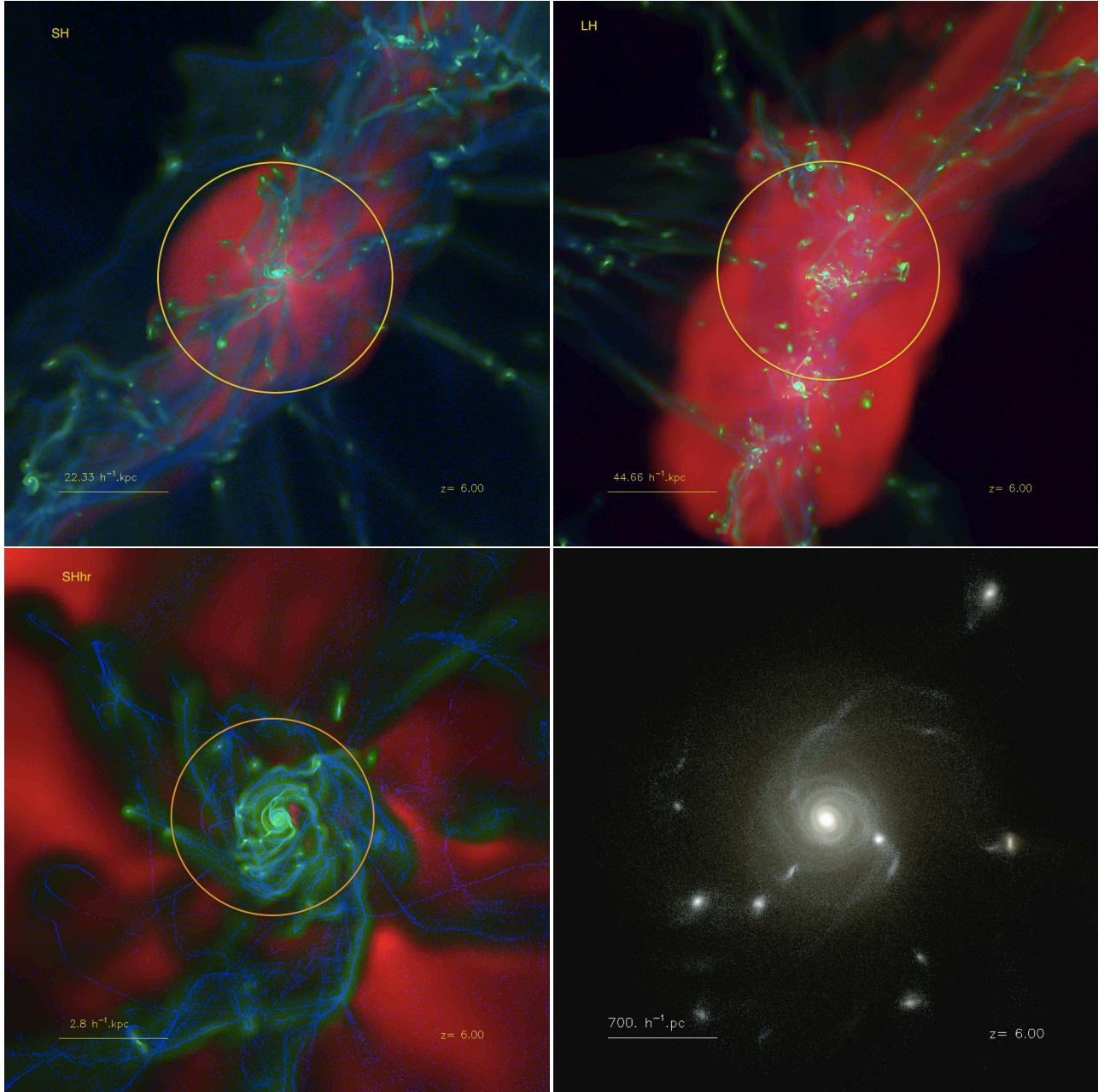
Figure 1. *Top panels:* Polychromatic view of the two halos in the SH and the LH simulation at $z = 6$. Gas density is color coded in green, gas temperature in red, and tracer particles in blue. The circles in the two top panels corresponds to the virial radius $r_{\rm vir}$. The *bottom left panel* displays the inner region of the top left panel simulated with higher resolution (SHhr), showing the transient disc and its connected filaments as discussed in the text. The circle corresponds to $0.1\,r_{\rm vir}$ (see table 1 for numerical values). The *bottom right panel* displays the stellar emission in the inner region of the bottom left panel as it would be observed in ugr filter bands. Note the compact bulge (the saturated spherical region at the centre) and the significant number of satellites flowing in along the cold streams on their way to merge with the central galaxy. Finally, we point out that even though in projection the hot gas phase seems to dominate, this halo is still mainly accreting cold gas.

the SH (and SHhr) simulation, and a 2048^3 grid for the LH simulation.

These simulations were run with the AMR code RAMSES (Teyssier 2002). The evolution of the gas was followed using a second-order unsplit Godunov scheme for the Euler equations. The HLLC Riemann solver with a first-order MinMod Total Variation Diminishing scheme to reconstruct the interpolated variables from their cell-centered values was used to compute fluxes at cell interfaces. Collisionless particles (dark

matter and star particles) were evolved using a particle-mesh solver with a Cloud-In-Cell (CIC) interpolation.

The initial mesh is refined with up to 9 levels of refinement. The maximum spatial resolution is chosen to be constant at a value $\Delta x = 95\,h^{-1}\cdot{\rm pc}$ in physical coordinates. We also performed a higher resolution simulation with 12 levels of refinement, corresponding to $\Delta x = 12\,h^{-1}\cdot{\rm pc}$ for the lower mass halo (SHhr). Grid cells are refined following a quasi-Lagrangian criterion if more than 8 DM particles lie in
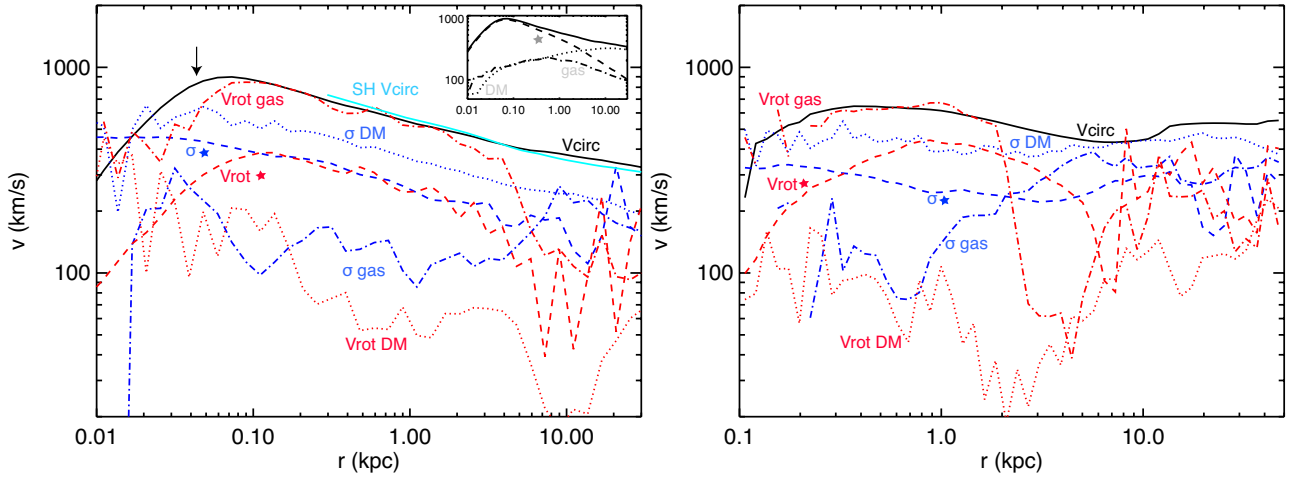
Figure 2. Circular velocities (black lines and inset), radial velocity dispersion (blue lines) and rotational velocities (red lines) of the DM (dotted lines), the stars (dashed lines), and the gas (dot-dashed lines) for the SHhr simulation (left panel), and the LH simulation (right panel) at $z = 6$. The blue line corresponds to the SH run. The bulge radius for the SHhr simulation is shown as a vertical arrow. At this redshift, these galaxies have the rotation curve of very compact ellipticals.
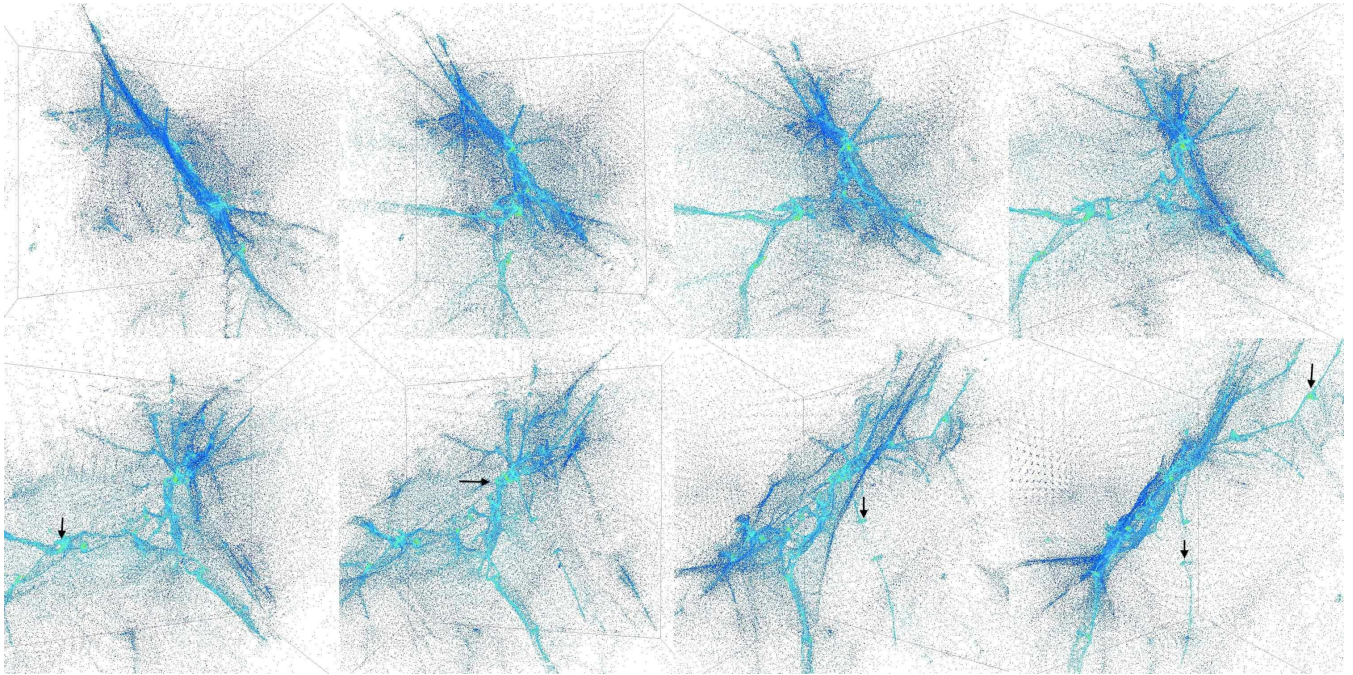

Figure 3. Distribution of tracer particles at $z = 9$ identified as belonging to the bulge of the SH halo at $z = 6$. *From top to bottom and left to right,* the observer is spiraling in towards the center of the web in the anti-clockwise direction around a vertical axis. The color coding represents the local log density of tracer particles (from blue: low density to yellow:high density). The size of the box is approximately 100 kpc across on the top left panel. The web-like filamentary structure of the gas distribution which ends up in the bulge is rather complex, though one filament embedded in a main wall dominates (best seen edge-on on the top left and bottom right panels). Note the disc-like features (marked by vertical arrows) which have formed perpendicular to the filaments. The forming bulge is marked by an horizontal arrow. We provide an animation which allows to better see this at `http://www.iap.fr/users/pichon/BH/`.

a cell, or if the baryon mass exceeds 8 times the initial dark matter mass resolution.

Gas cooling is implemented assuming a fixed metallicity of $10^{-3}Z_\odot$ with a Solar composition for the gas (Sutherland & Dopita 1993). Heating from the UV background follows Haardt & Madau (1996) with reionisation occurring at $z_{\rm reion} = 8.5$. The cooling module takes into account metal line cooling, allowing gas temperatures to reach a 100K temperature floor.

Star formation is assumed to occur in regions where the gas density reaches $n_{\rm H} > n_0 = 1\,{\rm H} \cdot {\rm cm}^{-3}$ for the SH and LH runs ($n_0 = 50\,{\rm H} \cdot {\rm cm}^{-3}$ for the SHhr run) and a random Poisson process is used to spawn star cluster particles (see Rasera & Teyssier 2006 and Dubois & Teyssier 2008 for more details). The star formation rate is assumed to scale accord-
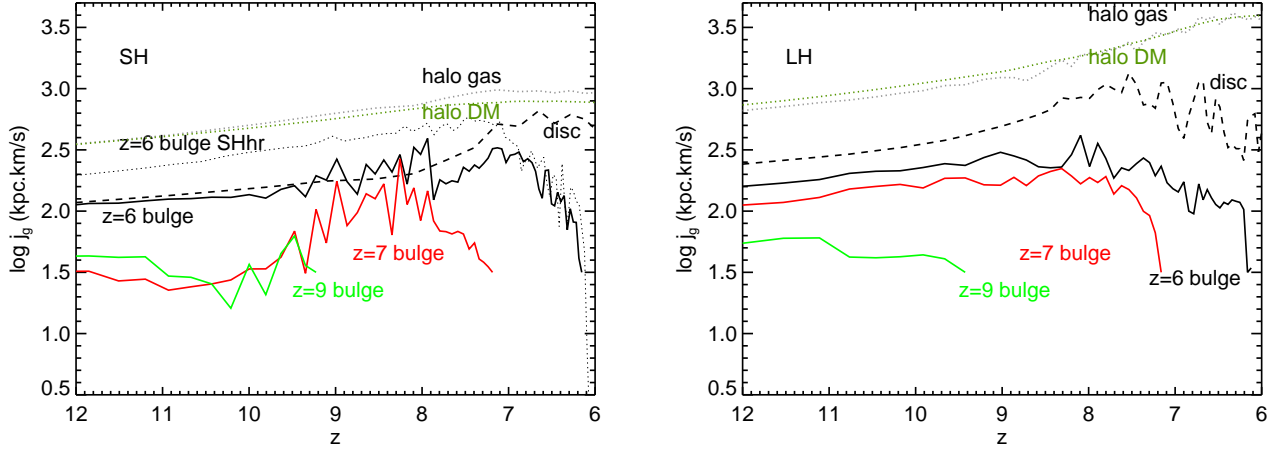
Figure 4. *Left panel:* Evolution of the specific angular momentum of the gas traced by the tracer particles identified to be part of the disc at $0.2 < r < 2\,\mathrm{kpc}$ in the SH simulation (dashed line), for tracer particles identified to be part of the bulge at $r \leqslant 0.2\,\mathrm{kpc}$ (solid lines) (or at $r \leqslant 0.04\,\mathrm{kpc}$ for the SHhr simulation, black dotted curve), and for tracer particles within r_rvir (grey dotted line) or DM particles (green dotted line) within r_rvir at $z = 6$. The bulge tracer particles are identified as falling into the bulge at $z = 6$ (black solid curve for the SH simulation, black dotted curve for the SHhr simulation), $z = 7$ (red curve), and $z = 9$ (green curve). The specific angular momentum is computed relative to the centre of mass of the ensemble of tracer particles (bulge, disc or halo) at a given time. *Right panel:* same as left panel for the LH simulation. The prominent drop in angular momentum is due to the cancellation of angular momentum of material streaming into the bulge from different directions. The larger drop in the SHhr simulation is due to the more efficient migration of clumps in the higher resolution simulation.

Table 1. Main properties of the SH, SHhr and LH simulations at $z = 6$. Stellar bulge versus disc masses are obtained with a bulge-disc decomposition of the stellar mass profiles. Gas and DM masses in the bulge and in the galaxy are measured at the radius where the stellar mass *effectively* reaches the mass inferred from the bulge/disc decomposition.

	SH	SHhr	LH
$M_\mathrm{vir}(\mathrm{M}_\odot)$	$5 \cdot 10^{11}$	$5 \cdot 10^{11}$	$2.5 \cdot 10^{12}$
$r_\mathrm{vir}(\mathrm{kpc})$	36	36	60
$V_\mathrm{vir}(\mathrm{km/s})$	245	245	425
$\Delta x(\mathrm{pc})$	135	17	135
$M_\mathrm{res}(\mathrm{M}_\odot)$	$1.3 \cdot 10^6$	$1.3 \cdot 10^6$	$1 \cdot 10^7$
$M_\mathrm{star}^\mathrm{bulge}(\mathrm{M}_\odot)$	$2.2 \cdot 10^{10}$	$1.9 \cdot 10^{10}$	$3.6 \cdot 10^{10}$
$M_\mathrm{star}^\mathrm{disc}(\mathrm{M}_\odot)$	$1.5 \cdot 10^{10}$	$2.9 \cdot 10^{10}$	$2.0 \cdot 10^{10}$
$M_\mathrm{star}^\mathrm{disc+bulge}(\mathrm{M}_\odot)$	$3.9 \cdot 10^{10}$	$5.6 \cdot 10^{10}$	$5.8 \cdot 10^{10}$
$M_\mathrm{gas}^\mathrm{bulge}(\mathrm{M}_\odot)$	$1.2 \cdot 10^{10}$	$1.0 \cdot 10^9$	$2.2 \cdot 10^{10}$
$M_\mathrm{gas}^\mathrm{disc}(\mathrm{M}_\odot)$	$2.8 \cdot 10^{10}$	$1.5 \cdot 10^{10}$	$2.9 \cdot 10^{10}$
$M_\mathrm{gas}^\mathrm{disc+bulge}(\mathrm{M}_\odot)$	$4.0 \cdot 10^{10}$	$1.6 \cdot 10^{10}$	$5.1 \cdot 10^{10}$
$M_\mathrm{DM}^\mathrm{bulge}(\mathrm{M}_\odot)$	$5.9 \cdot 10^9$	$1.1 \cdot 10^9$	$1.2 \cdot 10^{10}$
$M_\mathrm{DM}^\mathrm{disc}(\mathrm{M}_\odot)$	$5.5 \cdot 10^{10}$	$2.9 \cdot 10^{10}$	$1.1 \cdot 10^{11}$
$M_\mathrm{DM}^\mathrm{disc+bulge}(\mathrm{M}_\odot)$	$6.1 \cdot 10^{10}$	$3.0 \cdot 10^{10}$	$1.2 \cdot 10^{11}$
$\lambda_\mathrm{DM}(\mathrm{spin})$	0.048 ± 0.002	0.051 ± 0.002	0.107 ± 0.012

ing to the Schmidt-Kennicutt law $\dot{\rho}_* = \epsilon_* \rho / t_\mathrm{ff}$, where $\dot{\rho}_*$ is the star formation rate density, ϵ_* the star formation efficiency, and t_ff the local free-fall time of the gas. We set the efficiency of star formation to be $\epsilon_* = 0.01$ in good agreement with observed star formation surface densities in galaxies (Kennicutt 1998), and observations of local giant molecular clouds (Krumholz & Tan 2007). Star cluster particles are given a mass of $m_* = \rho_0 \Delta x^3$, with $\rho_0 = n_0 m_\mathrm{P} / X_\mathrm{H}$, m_P is the

proton mass, and $X_\mathrm{H} = 0.76$ is the Hydrogen fraction. The stellar mass resolution reaches $5.5 \cdot 10^4 \, h^{-1} \cdot \mathrm{M}_\odot$ for the low resolution simulations (SH and LH) and $5.5 \cdot 10^3 \, h^{-1} \cdot \mathrm{M}_\odot$ for the high resolution simulation (SHhr). We do not account for the effect of feedback due to supernovae (SNe) or AGN as we want to focus here on the infall of material from the cosmic web. We leave the effect of feedback for further work.

The top panels of fig. 1 show the setting of the gas around the two halos at $z = 6$. Most of the gas flows in cold along pronounced filamentary streams, and an accretion shock develops at the virial radius, increasing the amount of hot gas being accreted with time (Birnboim & Dekel 2003; Kereš et al. 2005; Ocvirk et al. 2008; Brooks et al. 2009; Dekel et al. 2009). The more massive halo in the LH simulation has a larger shock-heated region than the lower mass halo in the SH simulation, but nevertheless shows a cold filamentary accretion component penetrating the virial sphere as expected for this mass and redshift. Note that the stability of the shock is determined by the shape of the cooling curve and, thus, by the level of enrichment of the Intergalactic Medium (IGM) (Birnboim & Dekel 2003). Here, as we do not include any SN feedback, the value of the metal enrichment of the IGM is somewhat lower than what is expected, and the shock is more stable. However, SNe inject thermal energy to the surrounding gas and it is not clear how this would modify the stability of the shock. The bottom panels of fig. 1 are zooms of the high-resolution simulation SHhr which show a gravitationally central clumpy disc of gas (bottom left), and stars (bottom right). Note, however that as we will discuss later a significant fraction of the gas streams directly into the compact bulge at the centre without ever settling into a disc.

The black curves in fig. 2 show the contribution of gas, stars and DM to the circular velocity curves $v_\mathrm{circ} = \sqrt{GM/r}$ of the two halos while the red curves show the measured ro-

tational velocities, and the blue curves show the radial velocity dispersion. In both halos the baryons flowing to the centre become self-gravitating at a radius of about 3 kpc. The compact density distribution of the stars thereby leads to a significant inward rise of the circular velocity, with the rotational velocity (red dot-dashed lines) of the gas closely matching the circular velocity of the total mass distribution in the core of the halo $r < 0.1\,r_{\rm vir}$. The higher resolution SHhr simulation nicely resolves the peak of the rotation curve which reaches 900 km/s at a radius of 70 pc, that corresponds to a very compact bulge. Note that the upwards jump in the circular velocity curve for the LH simulation is due to the presence of a satellite galaxy at a distance of 15 kpc from the centre of the main galaxy.

We apply a bulge/disc decomposition by fitting two exponentially decreasing profiles on the the stellar surface density (see Appendix A of Dubois et al. 2012). This decomposition provides us with a stellar bulge (disc) mass $M_{\rm star}^{\rm bulge}$ (resp. $M_{\rm star}^{\rm disc}$). To infer the mass of gas (DM) into the bulge $M_{\rm gas}^{\rm bulge}$ (resp. $M_{\rm DM}^{\rm bulge}$), we measure the radius that encloses $M_{\rm star}^{\rm bulge}$ and compute the gas (resp. DM) mass content within this radius. We apply the same procedure for the total (disc+bulge) mass of gas (DM), and get the disc component by differentiating $M_{\rm gas}^{\rm disc+bulge}$ with $M_{\rm gas}^{\rm bulge}$ (resp. $M_{\rm DM}^{\rm disc+bulge}$ with $M_{\rm DM}^{\rm bulge}$). The central bulge contains 14, 24 and 41 % of the total baryonic mass for the LH, SHhr and SH simulation, respectively (see table 1). The gas fraction within it is 30 % for the two lower resolution and 5% for the higher resolution simulations. The decrease of the gas fraction with increasing resolution is expected due to denser clumps with lower free-fall time that form stars faster. Note that the stellar bulge rotates significantly faster than the DM but the rotational velocities are typically still a factor 2-4 lower than the circular velocity. The stellar bulge, while somewhat flattened is thus far from rotational support, and is supported by the radial velocity dispersion σ_*. At $0.1 < r < 2$kpc the compact central bulge is surrounded by a massive gravitationally unstable and rotationally supported gas disc. The stellar disc of the SHhr galaxy at $z = 6$ is supported by its rotation and its velocity dispersion, which explains its large disc scale height (~ 0.5 kpc) compared to the gas disc component (~ 0.1 kpc), and its old average formation time (243 Myr) compared to its dynamical time (3 Myr). The DM is essentially non-rotating and get its support against gravitational collapse from the radial velocity dispersion $\sigma_{\rm DM}$ of DM particles.

Let us close this section with a brief discussion how we will investigate the geometry of the cold gas inflow into the halos down to $z = 6$. We make use of massless *tracer* particles (e.g. Mitchell et al. 2009) to circumvent the difficulties that grid-based methods pose for following the Lagrangian path of the gas through the cosmic web into collapsed structures. In contrast to standard particles (DM or stellar particles), tracer particles are advected by using the updated velocity of the gas cells with the Riemann solver. Each tracer particle has its own velocity computed from a CIC interpolation. Tracer particles are uniformly distributed on the initial mesh of the simulation. We checked that the tracer particles rotational velocity profile closely matches its gas counterpart (see Appendix A). Figure 3 displays the particles of the SH simulation which are identified to belong to the bulge of the

central galaxy at $z = 6$ as they are distributed at $z = 9$. The filamentary origin of the bulge particles is very clear, confirming that a large fraction of the gas does indeed stream to the centre of the halos along the prominent filaments making up the cosmic web.

3   MASS ACCRETION AND ANGULAR MOMENTUM TRANSPORT IN THE HALO

3.1   Tracking the evolution of angular momentum

We are mainly interested here in the gas settling in the central region of the massive halos. This gas thus necessarily has low angular momentum. We therefore first compare the angular momentum of the gas falling to the inner bulge region of the galaxy (as defined by the scale length of the exponential fits performed for the bulge/disc composition: 200 pc for the SH and LH runs, and 40 pc for the SHhr run, see fig. 1) to that of the gas settling into the central disc surrounding the bulge.

In order to do this, we use the tracer particles to follow back in time the angular momentum of gas that ends up at a given redshift in either the central bulge or central disc and we calculate its specific angular momentum relative to the centre of mass, $\bar{\mathbf{r}}$, of the same (large) ensemble of tracer particles ($\sim 2.3\,10^5$ tracer particles located in the bulge of the SH galaxy at $z = 6$). The green, red and black solid curves in fig. 4 show the specific angular momentum evolution of gas identified in the bulge at $z = 9$, 7 and 6, respectively. Note that we have truncated the curves when the gas has reached the resolution limit of the simulation. The dashed curve is the evolution of the angular momentum of the gas that has settled into the surrounding disc with $0.2\,{\rm kpc} < r < 2\,{\rm kpc}$ at $z = 6$. We also show the specific angular momentum of the DM as well as the specific angular momentum of the tracer particles within $r_{\rm vir}$ at $z = 6$ in the two massive halos. In each case we have calculated the angular momentum as $j \equiv |\sum_i (\mathbf{r}_i - \bar{\mathbf{r}}) \times (\mathbf{v}_i - \bar{\mathbf{v}})|$. The mean angular momentum of the DM and the gas in the halo grow in reasonable agreement with tidal torque theory but, as discussed in detail by Kimm et al. (2011) and Pichon et al. (2011) in simulations with gas cooling, the angular momentum of the gas in the outer parts of the halo ($0.1\,r_{\rm vir} < r < r_{\rm vir}$) is higher than that of the DM by a factor of 2-4, decreasing with increasing mass or redshift and thus rareness of the halo. In our simulation we find a factor 2 difference similar to the more massive halos of Kimm et al. (2011) and Pichon et al. (2011). As shown by the dotted lines in fig. 4, the average specific angular momentum of the baryons (gas + stars) and DM within $r < r_{\rm vir}$ in the two halos is comparable.

The specific angular momentum of tracer particles ending up in the disc of the central galaxy also appears to grow in at late times. The specific angular momentum oscillates and globally decreases rather than increases due to gravitational perturbations (clump migration, mergers, etc.) which lead to inward mass and outward angular momentum transfer in part to the outer parts of the disk presumably, but most likely to the stellar and diffuse gaseous component of the halo. However, we are mainly interested here in the gas with the lowest angular momentum which forms the bulge. Initially the specific angular momentum of the gas ending up in this central bulge is lower than that settling into the disc,
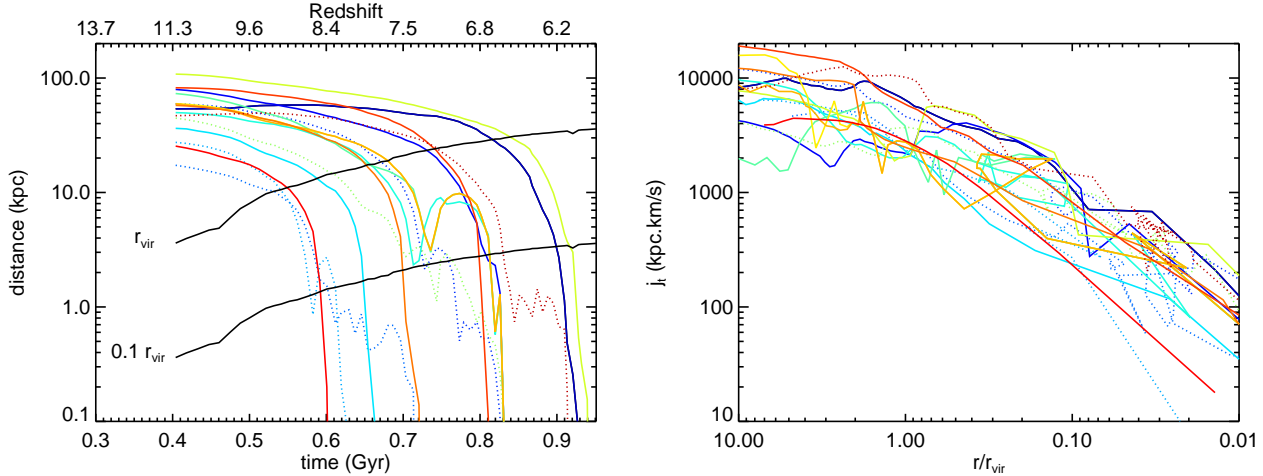
Figure 5. *Left panel:* Distance from the galaxy centre of 15 tracer particles randomly selected from the bulge tracer particles identified at $z = 6$ in the SHhr halo. Solid curves are for particles tracing matter directly accreted from the circum-galactic medium (CGM) into the bulge, whereas dotted curves trace matter accreted through the central disc. Solid black curves show r_{vir} and $0.1\,r_{\mathrm{vir}}$. Note that the tracer particles always rapidly sink as they enter r_{vir}, but sometimes linger in the CGM around $0.1\,r_{\mathrm{vir}}$. *Right panel:* specific angular momentum of the same tracer particles as in the left panel relative to the center of the bulge as a function of the distance to the center of the galaxy.

up to a factor two in the case of the more massive halo. At later times, when most of the mass actually assembles into the bulge, its evolution decouples from that of the central disc and its gas loses another factor $5 - 10$ in angular momentum.

In the following we use tracer particles to investigate in detail the trajectories of the flow of gas towards the bulge and discuss how it achieves sufficient angular momentum loss to settle into as compact a bulge as observed in our simulations.

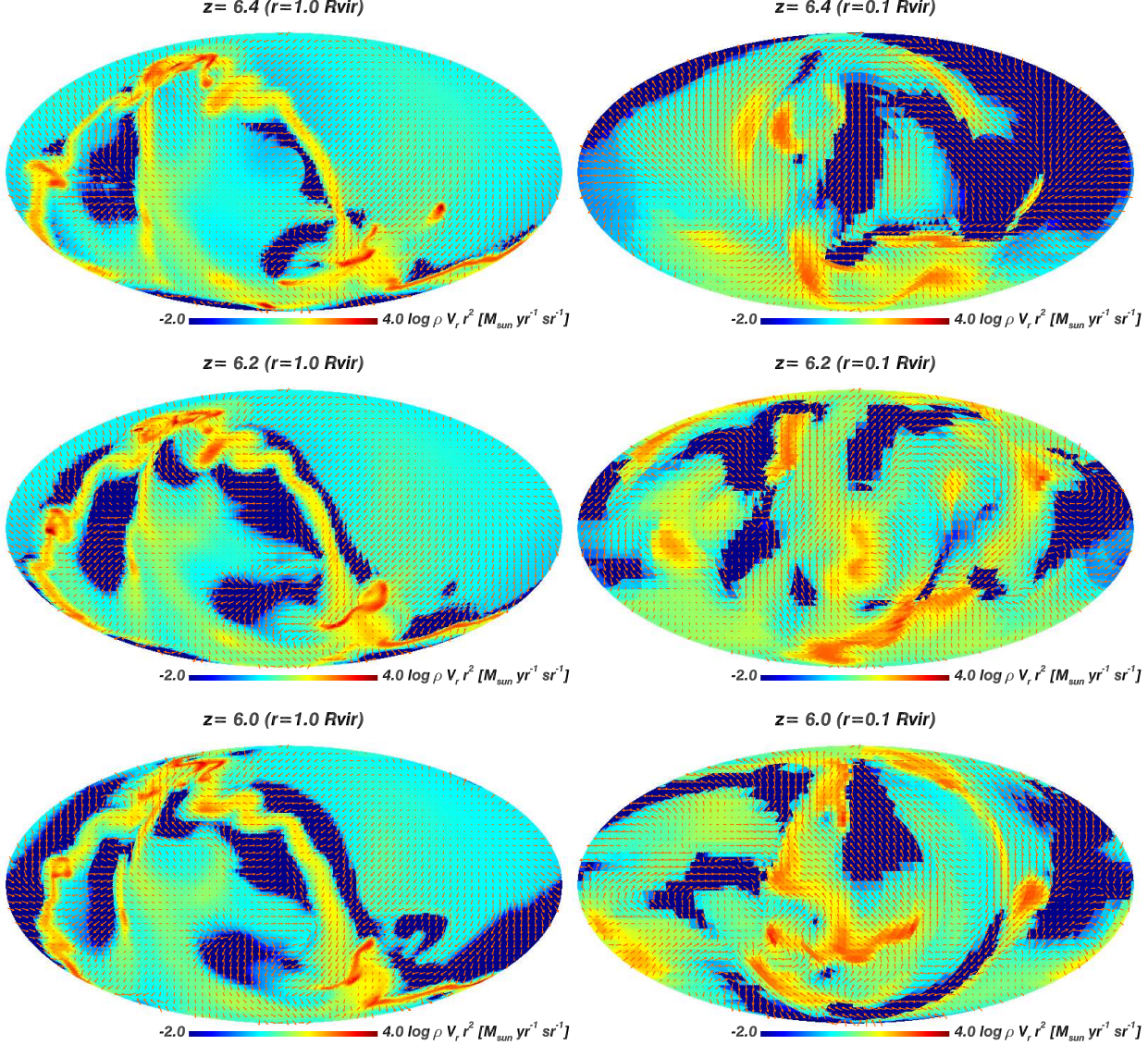### 3.2 Building up bulge from baryons in the cosmic web

Let us now take a closer look at fig. 3 and interpret it taking advantage of the fact that we can follow the trajectories of the gas flow using tracer particles. The ensemble of these particles ending up at the centre of the galaxy is initially distributed in a sheet-like structure within which is embedded a dominant filament. The tracer particles flow from this sheet into filaments where they form "protogalaxies". The gas in the sheet typically has a non zero impact parameter relative to the filament axis and protogalaxies thus acquire spin parallel to the filament in which they form (see also Codis et al. 2012). The gas then streams along these filaments into the dominant halo forming at the centre of the zoom region. These cold filamentary streams directly feed the central disc and bulge discussed in the last section. The protogalaxies falling in along these streams lead to minor mergers and are dragged in by dynamical friction and torquing. The (orbital and spin) angular momentum of the inflowing gas and that of the merging protogalaxies originating from different directions thereby add up incoherently (vector cancellation). Part of the inflowing matter directly feeds the compact bulge and another part settles temporarily into the surrounding disc. This is nicely demonstrated in the left panel of fig. 5 which shows the distance to the galaxy centre of 15 randomly chosen tracer particles ending up in the bulge at $z = 6$ as a function of time. The particles enter the halo and once they pass the virial radius, they quickly fall to the centre. A sizable frac-

tion of them hangs around $0.1\,r_{\mathrm{vir}}$ for a while and settles into this gravitationally unstable central disc, but more than half fall straight into the central bulge. We also see that the gas that settles into the bulge later in time comes from regions on the outskirts of the initial patch. The right panel of fig. 5 also shows that outside the virial radius of the halo, the particles that originated from further away generally tend to have a larger angular moment. The evolution of the angular momentum of the tracers has a significant stochastic component, but once they cross r_{vir}, these tracers of the bulge gas are seen to lose the angular momentum while sinking in.

Figure 6 shows the angular distribution of the mass influx at the virial radius on the left-hand side and deep within the halo at a tenth of the virial radius on the right hand side in the form of Mollweide maps (constructed using HEALPIX Górski et al. 2005) at three redshifts $z = (6.4, 6.2, 6.0)$. The maps also show the tangential velocity field in the form of arrows (the longer the arrow, the larger the tangential velocity). At the virial radius the angular pattern is very stable reflecting the inflow from the sheets and filaments constituting the large scale cosmic web. The tangential velocity field shows the expected drift of matter from voids into sheets/walls (the 2D bridges, e.g. north-west to south-east in left panels) and filaments (the 2D peaks on these maps Pichon et al. 2011; Danovich et al. 2012). In contrast, the flow at $0.1\,r_{\mathrm{vir}}$ is much more stochastic both in time and direction, and is a signature of a rapid redistribution/segregation of angular momentum within the collapsed halo (Kimm et al. 2011).

As a next step, let us now take a look at the geometry of the trajectories of the tracer particles as they stream together with the gas from the cosmic web into the bulge. In fig. 7 we show a selection of such trajectories starting at $z = 9$ for the SHhr simulation on three different scales as indicated on the plot. In the three panels a small subset of tracer particles are chosen randomly and are followed for a fraction of the remaining simulation time. Time increases from left to right panel. On large scales (at early times), we note that the flow is indeed dominated by the winding of

z= 6.4 (r=1.0 Rvir)   z= 6.4 (r=0.1 Rvir)

z= 6.2 (r=1.0 Rvir)   z= 6.2 (r=0.1 Rvir)

z= 6.0 (r=1.0 Rvir)   z= 6.0 (r=0.1 Rvir)

Figure 6. *Left panels:* Angular distribution of the mass flux of gas passing through the virial radius r_{vir} together with the tangential velocity field at $z = 6.4, 6.2$ and 6 (*from top to bottom*). Note the consistency of the characteristic patterns of sheets feeding the halo, with the largest inflow rates located at the position of the filaments, i.e. at the intersections of the sheets. Note also the coherent tangential velocity field on large angular scales with matter flowing away from the voids into the walls and along the filaments. *Right panels:* Same at $0.1\,r_{vir}$. The angular distribution at the smaller radius changes rapidly with time, reflecting the complex non-linear dynamics within the core of the halo. These maps are constructed from the high resolution SHhr simulation.

gas streaming from the main wall visible in fig. 3 around the main filament. The tracer particles start perpendicular to the filament within the walls. As they reach the filament, they take a (sharp) turn loosing their transverse motion and flow along the filament (left panel of fig. 7). This complex structure converges into a quite narrow and elongated "plait" on either side of the forming disc. The disc will advect further infalling gas at its periphery preferentially along its spin axis (middle panel of fig. 7). The gas falling towards the disc from the Circumgalactic Medium (CGM) also shocks as it approaches the disc and takes (another) sharp turn aligning itself with the (transient) spinning disc. This flow drags along satellites (collapsed structures/proto-galactic clumps that formed outside

the halo in the cosmic web) and cold filamentary non-star forming gas (right panel of fig. 7).

3.3 The radial evolution of fluxes

Let us define different phases for the gas: the star forming gas with $\rho \geqslant \rho_0$, the hot diffuse gas phase with temperature $T \geqslant 10^5$ K and $\rho < \rho_0$, the cold filamentary phase with $T < 10^5$ K and $100\,\bar{\rho}_b \leqslant \rho < \rho_0$ ($\bar{\rho}_b$ is the average baryon density of the Universe), and the cold diffuse phase with $T < 10^5$ K and $\rho < 100\,\bar{\rho}_b$. A careful inspection of the mass flux at $0.1\,r_{vir}$ and r_{vir} shows that the infall in the SHhr halo is largely dominated by the cold filamentary (non-star forming) gas with high accretion rate $\dot{M}_{acc} = 100 - 200\,M_\odot$ (left
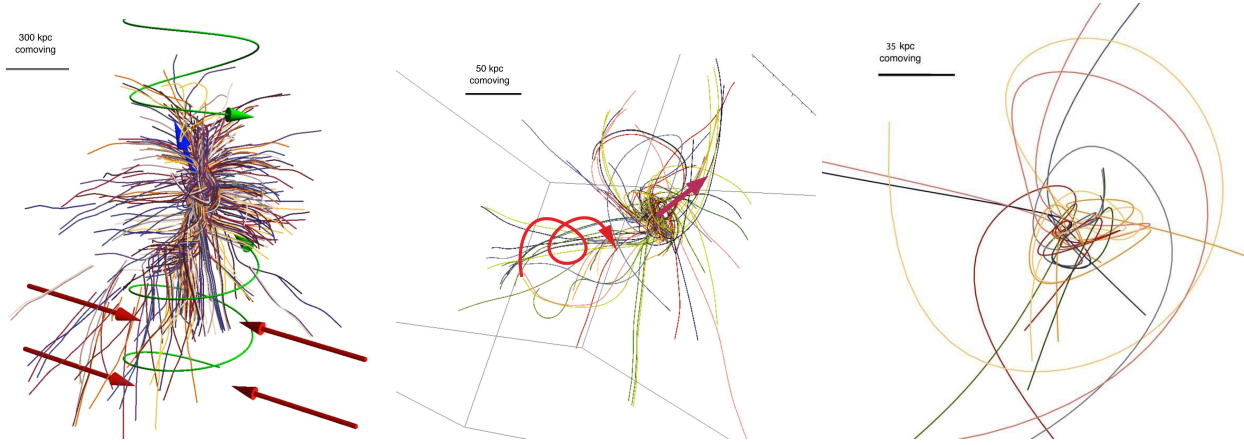
Figure 7. The trajectories of bulge tracer particles in the outer region (*left panel*) on intermediate scales (*middle panel*) and in the inner region of the halo (*right panel*). On super halo scales, the gas flows out of the voids into the the walls/sheets (red arrows) and winds around the filaments (*green arrows*, see also fig. 6). The gas and proto-galactic clumps flow along the filaments and merge with the most massive clump which will later become the compact central bulge (*middle panel*). A large fraction of the gas is funneled directly to the compact bulge at the centre, while the rest settles briefly into the surrounding disc. The disc gets continuously disturbed by merging clumps and is thus unstable and transient. As a result, the gas in the disc rapidly loses angular momentum and contributes to the growth of the gas rich bulge (*right panel*; the horizontal bar corresponds to the Virial radius of SHhr at $z = 6$).

and right panels of fig. 8), high enough to bring sufficient amounts of gas that drives a recurrent Toomre unstable disc (bottom left panel of fig. 1) with typical Toomre parameter of the order of $Q \sim 1$ in the central galaxy of the SHhr simulation (see also Dekel et al. 2009; Ceverino et al. 2010). Multiple clumps are observed in the disc and very few are accreted through mergers (*ex situ*). When measured at r_{vir} for the SHhr halo at $z = 6$, 10 % of the total accreted mass of gas is in the form of compact star forming clumps, 55 % is accreted through cold streams, and the rest 35 % is a diffuse accretion. This proves that clumps form within the galaxy (*in situ*) via strong disc instabilities (see also fig. 9 below). This process occurs generically, but for rare peaks, the larger number of connected filaments, and the importance of minor merger accelerates the radial migration. This rapid inflow of fresh gas is the result of comparable levels of accretion at r_{vir}, which suggests that the gas falls quickly into the center of the halo from large distance in a time comparable to the halo free-fall time. The clumps that are formed *in situ* migrate rapidly inwards while releasing their residual angular momentum to the stellar component surrounding the bulge (Immeli et al. 2004; Elmegreen et al. 2008; Bournaud et al. 2011).

### 3.4 Inflow through the disc *versus* direct CGM infall

We now investigate how much gas flows directly from the CGM into the bulge and how much gas passes through the central disc surrounding the bulge first. We define disc[1] tracer particles that have passed through the disc surrounding the bulge before settling into the bulge as those that have stayed at a distance $r_{b} < r < 0.1 r_{vir}$ (where the scale length of the bulge $r_{b} = 200$ pc for the SH and LH runs, and $r_{b} = 40$ pc for the SHhr run) for a time t_{acc} larger than the time required to complete a full rotation at $0.1 r_{vir}$, $t_{circ}(0.1 r_{vir}) = 2\pi(0.1 r_{vir})/v_{circ}(0.1 r_{vir})$, with $v_{circ}(0.1 r_{vir})$ being computed

from the mass of gas, stars, and DM at $0.1 r_{vir}$. Looking again at the selection of tracer particles shown in fig. 5, most of the bulge tracer particles accreted from the CGM fall very rapidly into the bulge, with a few that appear to have their trajectories perturbed during their infall but *before* reaching the disc ($0.1 r_{vir}$). Some other tracer particles hang around in the disc for some time *after* reaching $0.1 r_{vir}$ at an almost constant distance from the centre before being accreted into the bulge. These latter particles are the ones which migrate from the disc to the bulge.

This is further quantified in fig. 10 which shows number counts of tracer particles identified as belonging to the bulge at $z = 6$. The figure shows how much time t_{acc} (as a function of t_{circ}) the tracer particles spend at radii $r_{b} < r < 0.1 r_{vir}$ as a function of the time before they reach r_{b}. The time to complete one rotation at $0.1 r_{vir}$, t_{circ}, increases with time, thus, the increase seen in fig. 10 corresponds to a net increase of accretion time for baryons before being accreted into the bulge. Tracer particles which are accreted earlier fall rapidly into the bulge, while particles accreted later spend more time within the disc. Indeed, the particles accreted later have typically a larger angular momentum modulus (Pichon et al. 2011), hence are expected to settle into the disc before they reach the bulge. This pattern is the same for all three simulations: for any given patch of material, late-time infalling material does so with increasing angular momentum.

We now measure the evolution of the average relative accretion time with redshift $t_{acc}/t_{circ} = \tau(1 + z)^{\alpha}$ for our three different simulations. We find $\tau = 3.4, 3.1, 1.4$ and $\alpha = -3.6, -3.4$, and -1.6 for the SH, SHhr, and LH halos respectively. In the most massive LH halo, we clearly have shorter relative accretion time compared to the lower mass SH halo (middle panel of fig. 10), suggesting that the bulge in this most massive structure acquires more gas by direct infall from the CGM. For the smaller mass halo, in the high resolution simulation SHhr, the particles have slightly shorter accretion times than the low resolution simulation SH. The SHhr simulation is able to follow the formation of

---

[1] Note that this definition differs from that given in fig. 4.
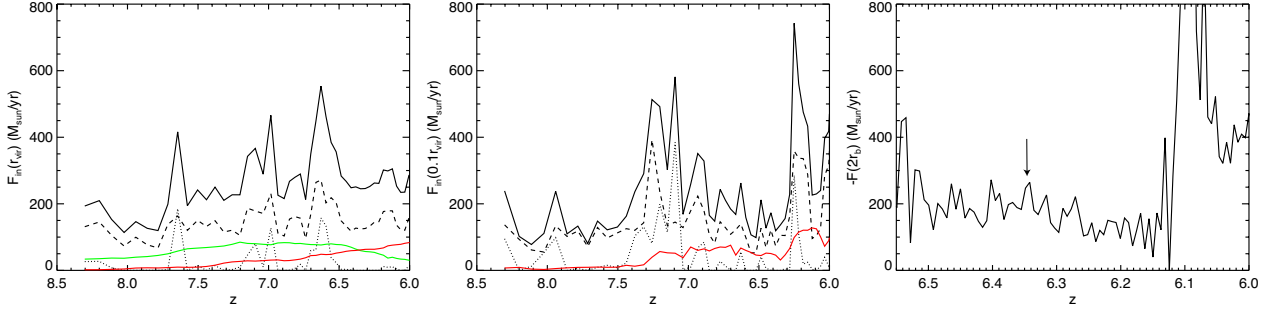
Figure 8. *Left panel*: inward flux measured at $r_{\rm vir}$ for the SHhr simulation for the star-forming gas (dotted line), the cold filamentary gas (dashed line), the cold diffuse gas (green line), the hot shock-heated gas (red line), and the total (solid line). *Middle panel*: same as the left panel measured at $0.1\,r_{\rm vir}$. The gas is essentially accreted through cold infall (diffuse and filamentary) at $r_{\rm vir}$, and through cold filaments at $0.1\,r_{\rm vir}$, with very few star-forming clumps contributing to the overall mass infall. *Right panel*: net inward flux ($-F = -(F_{\rm in} + F_{\rm out})$) measured at twice the bulge radius $2r_{\rm b} = 80$ pc. The gas entering the bulge of the galaxy is composed of star-forming clumps with a bursty accretion of gas. The vertical arrow marks the burst corresponding to the accretion event seen in fig. 9. The massive burst of accretion at $z = 6.1$ corresponds to the capture of a satellite galaxy.
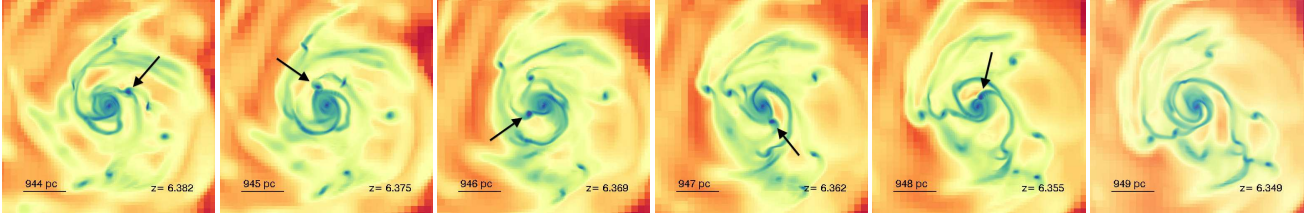
Figure 9. Time sequence (*from left to right*) of the gas density evolution in the central SHhr galaxy illustrating the migration of a dense clump of gas (indicated by the black arrow) into the central bulge. This radial migration of *in situ* clumps is consistent with the inflow burst of figure 8 (right panel, vertical arrow).

smaller clumps which have shorter accretion times than matter falling in diffusely. This is in agreement with clumps in the galaxy having shorter migration times towards the bulge than gas being accreted by secular disc instabilities such as bars, or spiral arms (Bournaud et al. 2005, 2011).

If we similarly consider the time it takes for these particles to travel from the virial radius, $r_{\rm vir}$, to the disc, $0.1\,r_{\rm vir}$, it becomes apparent that these same particles on average never complete one full rotation corresponding to $t_{\rm circ}(r_{\rm vir})$ ($\tau = 0.6,\ 0.3,\ 0.8$ and $\alpha = -1.5,\ -1.1$, and -1.6 for the SH, SHhr, and LH halos, see right panel of fig. 10). In fact, it takes them a time comparable to the halo free-fall time ($t_{\rm ff}{=}t_{\rm circ}/\sqrt{32}$) to reach the galaxy. For these massive halos at high redshift, the gas that makes up the compact bulges is brought in from the IGM almost directly. This is in good agreement with our previous finding that the accretion rate at $0.1\,r_{\rm vir}$ is comparable to the accretion rate at $r_{\rm vir}$ (see fig. 8).

We can now define gas as flowing directly into the bulge from the CGM as gas for which the time to reach the bulge from $0.1\,r_{\rm vir}$ is smaller than the time to make a full revolution at $0.1\,r_{\rm vir}$ *i.e.* $t_{\rm acc} < t_{\rm circ}$. Correspondingly for gas flowing into the bulge through the disc driven inwards by disc instabilities, $t_{\rm acc} \geqslant t_{\rm circ}$. Figure 11 shows that the fraction of baryons accreted directly from the CGM into the bulge defined in this way is dominant early on and decreases to about half by $z = 6$. Disc instabilities are increasingly important for the feeding of the bulge component of the galaxy at late times. This is in good qualitative agreement with the prediction of Pichon et al. (2011): early infalling gas has very low angular momentum, and can directly supply the fuel for

the growth of the massive compact bulge, gas accreted at late times coming from larger distance in the IGM and with higher angular momentum contributes to the formation of a compact and gravitationally unstable disc. This is consistent with the disc size evolution with time (increased angular momentum), that grows from 100 pc at $z = 9$ to 350 pc at $z = 6$ in the SHhr simulation. The total baryonic mass accreted into the bulge, as indicated by the amount of tracer particles accumulated into this compact region, is larger than the total mass of gas plus stars measured at $z = 6$ into the bulge by a factor $1.5 - 3$ (table 1). As the tracer particles do not account for the amount of gas mass lost to star formation and that stars can be expelled from the compact bulge by mergers, tidal stripping, etc., more than the gas we systematically over-estimate the amount of baryons ending up in the bulge with this method.

Still, there clearly is a sufficient amount of gas in the bulge at all times to potentially feed a very massive BH with mass $\sim 10^9\,{\rm M}_\odot$ (see numbers in table 1). The BH mass to bulge mass ratio $\Gamma = M_{\rm BH}/M_{\rm bulge}$ evolve with redshift as seen in observations (Decarli et al. 2010; Merloni 2010) and predicted by cosmological simulations (Di Matteo et al. 2008; Booth & Schaye 2011; Dubois et al. 2012). With the extrapolation of the observational fit from Decarli et al. (2010) (obtained between $0 < z < 3$) up to $z = 6$ ($\Gamma = 0.096$), we expect the BH mass to be $M_{\rm BH} \sim 2 \cdot 10^9\,{\rm M}_\odot$. The amount of gas in the bulge of the SHhr galaxy at $z = 6$ could seem insufficient to feed a BH as massive as $2 \cdot 10^9\,{\rm M}_\odot$. However, the accretion and consumption of gas onto the BH is in competition with the consumption of gas through the star formation process,
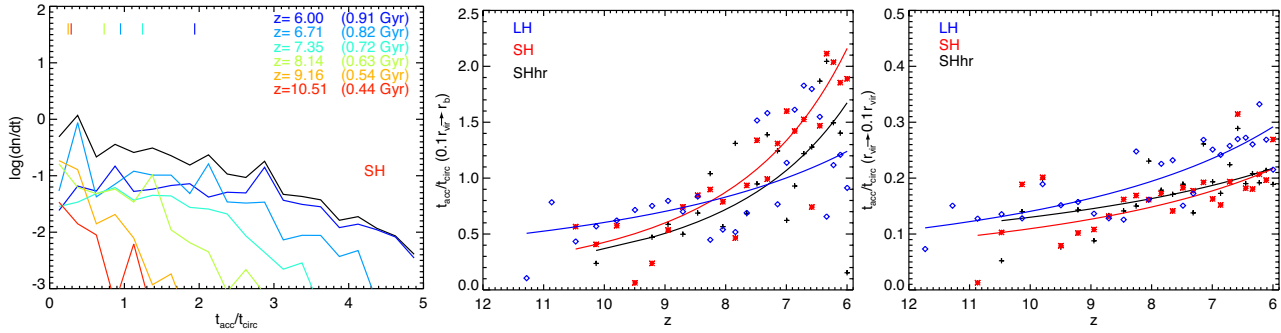
Figure 10. *Left panel:* The number of tracer particles identified in the bulge at $z = 6$ in the SH simulation as a function of the time (normalized to $t_{circ}(0.1\,r_{vir})$) spent at radii $r < 0.1\,r_{vir}$) for different accretion redshifts as color coded on the plot. The vertical ticks correspond to the average accretion time for tracer particles entering the bulge at the corresponding redshift. *Middle panel:* average normalized accretion time of bulge tracer particles at $z = 6$ to travel from $0.1\,r_{vir}$ to r_b. The number of completed orbits spent in the disc is still rather small (less than 2). As expected, the later the infall, the larger the number of completed orbits. *Right panel:* same as middle panel but to travel from r_{vir} to $0.1\,r_{vir}$ for the three different simulations, LH (blue diamonds), SH (red stars), and SHhr (black plus). Particles travel in the halo very quickly in less than a fourth of a rotation (i.e. in a free-fall time).

and a non-negligible amount of gas that is turned into stars could be captured by the central BH if there was any.

When measuring the gas mass flux around the galactic bulge in the SHhr galaxy (right panel of fig. 8), it becomes evident that the accretion is very irregular and proceeds by bursts of very dense clumps of gas, with a high level of $\sim 200\,M_{\odot}/yr$ gas accretion rate towards the bulge maintained. Such a mode of accretion onto the bulge is illustrated in fig. 9, where we can observe a dense clump of star-forming gas migrating into the center of the galaxy and being absorbed by the bulge. From this stochastic accretion mode, we expect the central AGN to release energy in rapid bursts interspersed with longer periods of very little activity. Capture of galaxy satellites (burst of accretion at $z = 6.1$) are rarer events that bring huge amounts of gas ($> 1000\,M_{\odot}/yr$) and can potentially disperse all the galactic gas while triggering a strong AGN activity (Di Matteo et al. 2005).

3.5 How the gas loses angular momentum to form bulges

If we look back at the angular momentum evolution plotted in fig. 4, we realise that bulge tracer particles sample material which has a factor ~ 3 less specific angular momentum to begin with in the LH run than the average specific angular momentum of the baryons in the halo. This is obviously a segregation effect. Amongst all the material flowing into the halo, it is the early infalling low angular momentum gas that preferentially settles (and much of this directly from the CGM) into the bulge as discussed extensively in the last section and in Pichon et al. (2011). This is, however, not quite sufficient to explain the factor 10-30 lower angular momentum of the gas and stars in the bulge. The right panel of fig. 5 shows how the angular momentum of the ensemble of tracer particles which we have discussed earlier lose their angular momentum as they sink to the central bulge. The angular momentum loss is complex with some of the particles losing it rather gradually, but there are also sudden drops by factors of a few, indicative of what we may call angular momentum cancellation, followed by smaller gains of specific angular momentum.

In the left panel of fig. 12 we compare the PDF of the pro-

jected angular momentum of bulge tracer particles at $0.1\,r_{vir}$ at $z = 6$ with the angular momentum of tracer particles at r_{vir} (van den Bosch et al. 2002; Sharma & Steinmetz 2005).

As discussed by Kimm et al. (2011), if the gas is allowed to cool, this specific angular momentum distribution becomes very broad. A significant fraction of the baryons is actually rotating in the direction opposite to the overall rotation of the halo. Filaments and clumps of material with very different angular momentum orientation will reach the centre in turn, with low specific angular momentum material getting there first. This explains why in the right hand panels of fig. 6 the angular distribution of the mass influx changes rapidly with time deep inside the halo. The figure clearly demonstrates that the randomly oriented angular momentum of the material that reaches the bulge cancels each other out resulting in a steep spike around zero in the PDF of the angular momentum. This together with the usual means of losing angular momentum like the transfer between spin and orbital angular momentum, dynamical friction acting on inspiraling clumps and gravitational instabilities (bar-like and clumping) in the disc results in a very compact but nevertheless only moderately rotating bulge. Note that a similar "cancellation" of angular momentum is seen as the tracer particles approach the halo (right panel of fig. 12).

3.6 What is different in rare halos?

Why is this angular momentum segregation so efficient in the two massive rare halos we have studied here? To answer this properly would require a systematic study of a wider range of halo masses and redshifts. Here we formulate a brief argument based on a comparison with the previous work Kimm et al. (2011) and Pichon et al. (2011).

Expanding locally on the work of Bond et al. (1996), these authors showed that the large scale distribution of the angular momentum in a collapsing patch produces a consistent secondary inflow: gas is draining out of the prominent surrounding voids in the cosmic web, into the sheets and filaments before it finally gets accreted onto virialised halos along cold flows. As these sheets/filaments constitute the boundaries of generally asymmetric voids, they acquire a net
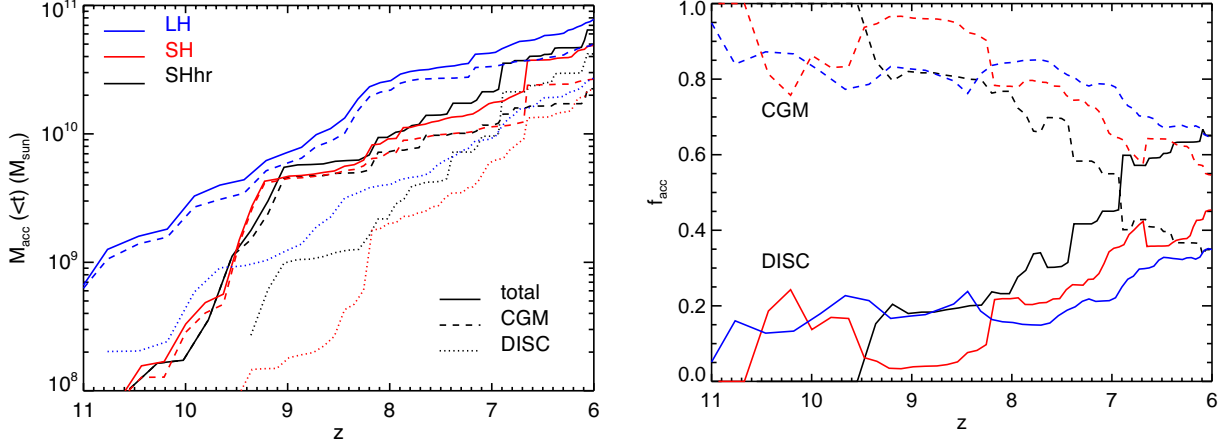
Figure 11. *Left panel:* Cumulative mass of gas (tracer particles) accreted into the bulge as a function of cosmic time, for gas directly accreted from the CGM (dashed curves) and gas accreted through a disc instability (dotted curves). Blue curves correspond to the SH, red curves to the LH and black curves to the SHhr simulations. *Right panel:* Fraction of tracer particles accreted directly from the CGM (dashed curves) or through the disc (solid curves). The color coding is the same as for the left panel. At high redshift infall is predominantly directly from the CGM, while by redshift $z = 6$, about half of the particles spend more than one $t_{circ}(0.1 r_{vir})$ in the disc.
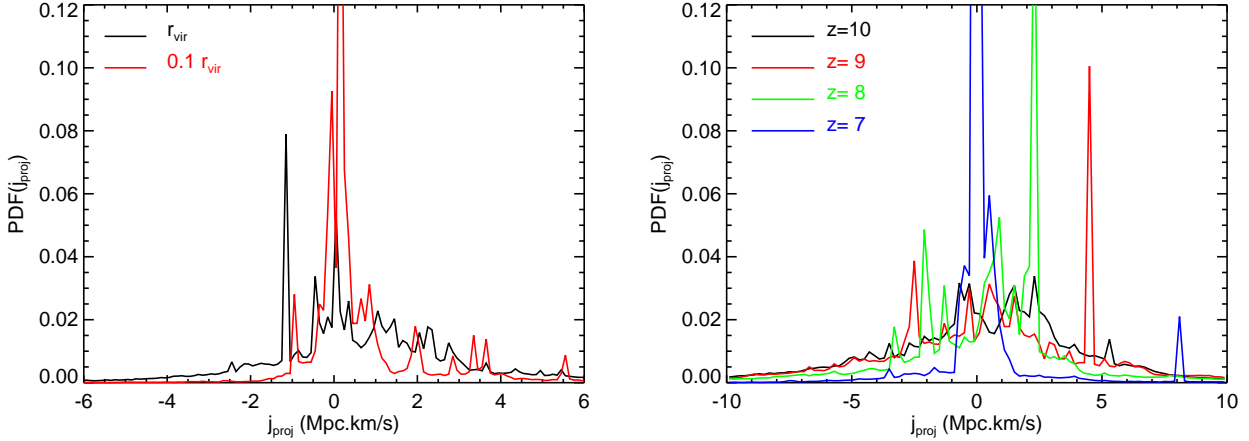
Figure 12. *Left panel:* PDF of the projected specific angular momentum of bulge tracer particles of the SH simulation selected at $z = 6$ at the virial radius (black line) and at $0.1 r_{vir}$ (red line). The specific angular momentum of each particle is projected along the normalized specific angular momentum of the patch containing all tracer particles in each region. The specific angular momentum is computed relative to the centre of the bulge. Note the overall contraction of the angular momentum distribution towards the centre of the halo. *Right panel:* PDF of the projected specific angular momentum of the tracer particles of the bulge at $z = 6$ along the angular momentum of the patch for different redshifts $z = 10$ (black line), $z = 9$ (red line), $z = 8$ (green line), and $z = 7$ (blue line). The specific angular momentum is computed relative to the centre of mass of the patch of bulge tracer particles. Note again the contraction of the accumulated angular momentum PDF as a function of cosmic time.

transverse motion relative to their host halo, which becomes the seed of the advected angular momentum along filaments. They argued that this large-scale driven consistency explains why cold flows are so efficient at building up discs from the inside out. Kimm et al. (2011) and Pichon et al. (2011) also reported using the MareNostrum hydrodynamical simulations (Ocvirk et al. 2008) that, unlike that of DM[2], the spin parameter of the baryons decreases (i) as the halo mass increases and (ii) as redshift increases for a halo of fixed mass (in their fig. 4

for the angular momentum flux of the gas at the virial radius, and in fig. 8 of Kimm et al. (2011) for the specific angular momentum of the gas within $0.1 r_{vir} < r < r_{vir}$). This suggests a decrease of the overall gas spin parameter for rarer (and thus more massive halos).

Therefore we now argue that with the formation of the very compact bulges in the extremely rare halos that we studied, we see a continuation of this trend which feeds through to the angular momentum segregation and cancellation during the non-linear evolution ("collapse") of the halo. In other words, the gas streaming cold to the centre avoids significant mixing in the outskirts of the dark halo. It thus inher-

---

[2] though Knebe & Power (2008) report a small trend of spin parameter decreasing with halo mass at high redshift

its the decrease of spin parameter of the gas with increasing rareness of the density peak seeding the formation of the halo.

This trend is expected on theoretical grounds. Indeed, Pichon et al. (2010), (fig. 4, bottom panel) demonstrates that in Lagrangian space (corresponding to the large redshift Gaussian initial conditions for structure formation), the rarer the peak, the larger the number of filaments connected to it (as the high contrast requires large negative curvature in all directions, which implies isotropy of the peak; this isotropy allows for connections to filaments from all directions). Hence we would expect that the larger number of connected filaments lead to more efficient cancellation of their specific angular momentum resulting in a low overall spin for the bulge. Part of this cancellation already occurs on large scales in the cosmic web during shell crossing of the DM in the cosmic walls/sheets and filaments, and continues when the gas with the low angular momentum advected along the filamentary streams reaches the bulge at the centre of the halo. Note that tidal torque theory also predicts a weak anti-correlation (Heavens & Peacock 1988) between the spin parameter and the mass of halos, as the amount of torquing between a rare density peak and its (more spherical) tidal field decreases with the rareness of the peak. For the baryons, this anti-correlation is amplified by the shock-induced segregation which takes place in the cosmic web (walls, filaments).

Let us revisit the early stage of the bulge formation in our simulations in view of these theoretical priors. First, the low angular momentum cold gas streams right along a couple of filaments into the seed of a bulge. Gas falling in later along other filaments is unlikely to have low angular momentum with respect to that frame (and typically will have larger angular momentum amplitude) so will recurrently form a transient disc. This disc gets disturbed by minor mergers which also sink-in via angular momentum loss with the stellar component at these radii. The competing effects of disc formation and disc disruption depend on the rareness of the peak as well as cosmic time. The rarer the peak, the lower the spin parameter of the advected gas. The later the infall of the gas, the larger the amount of advected angular momentum. The two halos in our SH and LH simulations are rather extreme examples in terms of rareness and appear to confirm this picture. Hence the formation of the very compact galactic bulges in the two simulations corresponds to the early stage where low angular momentum gas streams directly to the bulge and the rotationally supported disc is small and constantly destroyed and recreated. The later stages, when higher angular momentum gas accumulates and settles into a robust disk as described in Pichon et al. (2011), may occur later depending on the nature of the Lagrangian peak. For very rare massive halos such as those simulated here, the opportunity to reach this second stage has not occurred by redshift $z = 6$.

4 DISCUSSION

4.1 Limitations and Caveats

We would like to stress again that we have performed in this paper an exploratory study which consists in the analysis of high resolution simulations of only two massive halos. These simulations *do not* include any model for the growth of a central BH, and perhaps more importantly neither AGN nor stellar feedback. We have mainly concentrated here on describing some of the physical mechanism of the inflow of gas in these massive halos with a particular emphasis on the role played by angular momentum. AGN (and stellar) feedback together with the effect of changing the details of star formation in the simulations are probably the most important factors that would impact the results of our study.

In particular, spherical winds driven by radiative pressure could dramatically alter the flow of the cold filamentary accretion once the BH has become sufficiently massive and may – at least in principle – prevent the stellar bulge from becoming as tightly bound and massive as we found in our simulations. A simple calculation of the potential effect of AGN feedback on the binding energy of the bulge component shows that a $M_{BH} = 10^9 M_\odot$ BH has enough energy $E_{AGN} = \eta \times 0.1 M_{BH} c^2 = \eta \times 2 \cdot 10^{62}$ ergs to efficiently remove all baryons from the bulge with a total energy of a few 10^{59} ergs, even considering low conversion efficiency of AGN luminosity into mechanical energy output (e.g. $\eta = 0.01$). It is, however, not obvious what level of feedback would be needed to stop the accretion flow, because observed AGN feedback is often focused into a small/moderate solid angle (blazars, jets) and may therefore not significantly impact the cold filamentary accretion or the capture of star-forming clumps (as illustrated in fig. 9). It is also not obvious to what extent feedback schemes currently implemented in numerical simulations actually properly capture the coupling of the released energy and momentum to the interstellar and circumgalactic media. This problem will thus not be straightforward to address, and we postpone this issue to a future study of the impact of AGN feedback on the gas inflow onto the central BH by testing different modes of AGN feedback (collimated jets or spherical winds following the Dubois et al. 2012 model). The detailed mode and efficiency of star formation will also strongly affect how compact the bulge will become (Agertz et al. 2011) and, more importantly, how much gas will be left over for the feeding of the central supermassive BH.

Last but not least, there are still numerical issues with the sinking of cold gas in hot gaseous atmospheres, which in the past have led to the formation of overly prominent galactic bulges. This appears to be, however, a more serious problem for SPH codes than for AMR-based hydrodynamical codes like RAMSES (Torrey et al. 2011; Scannapieco et al. 2011). The fact that RAMSES simulations of more common halos at lower redshifts with a very similar setup to ours result in prominent extended disc and moderately dominant and less compact bulges provides some reassurance here. We hope to be able to report progress on some of these issues in a forthcoming study.

4.2 Implications for the formation/build-up of compact bulges and their central supermassive BHs

The most striking result of our simulations is the large fraction of gas that settles into a very compact bulge. In fact the circular velocity of the bulge significantly exceeds the circular velocity of the host halo and with a circular velocity of 900 km/s is significantly larger than that of even the most massive galactic bulges at low redshift. The ab-

sence of such strongly bound galactic bulges in the nearby Universe is not necessarily an observational concern. As we have discussed earlier, only about a ten thousand or less of such objects are expected to have formed in the whole Universe. Furthermore, such an ultra-compact central region would not be easy to detect in a much larger and more massive galactic bulge surrounding it. It may in fact be mistaken as the direct signature of a central BH. A strong evolution of the characteristic sizes of galactic bulges is actually observed. Galactic bulges appear to be about a factor 3-5 smaller at $z \sim 2-3$ (Daddi et al. 2005; Cimatti et al. 2008; van Dokkum et al. 2008; Whitaker et al. 2012; Oser et al. 2012) than they are at $z = 0$. Measuring stellar velocity dispersions at these redshifts is very difficult and expensive in terms of telescope time but there is the intriguing case described by van Dokkum et al. (2009) with a claimed velocity dispersion of 510 km/s at $z = 2.1$. At the redshifts we are considering here ($z \sim 6$) the only observational data probing the depth of the potential wells of the galaxies hosting the billion solar mass BHs are a few CO measurements with rather low velocity width (Wang et al. 2010), but it is far from clear to what extent this actually probes the depth of the central potential well of the galactic bulge presumably hosting these supermassive BHs.

With the resolution of our simulation there is still some way to go to reach the sphere of influence even of a billion solar mass BH but there is definitely enough low angular momentum gas funneled to the centre to build-up the masses reported for the most luminous QSOs at $z \sim 6-7$. In fact if we take the the circular velocity of the galactic bulges in our simulations at face value, a non-evolving $M_{\rm BH}/\sigma$ - relation would predict BHs well in excess of ten billion solar masses. More important is that the gas arrives at the centre continuously as required to explain the sustained gas supply at close to the Eddington rate over cosmological timescales which has also been reported by Sijacki et al. (2009) and Di Matteo et al. (2012) from their simulations. As we have discussed, a significant fraction of this gas streams straight into the bulge without ever properly settling into a disk. In fact a fraction of the gas actually streams straight into the centre of the bulge as defined by the resolution limit of our simulations. This gas spirals inwards in about two dynamical times from a tenth of the virial radius and while the streams carrying the gas into the halo are aligned in a preferred plane at large radii, at small radii the inflow is largely coming from random directions in good agreement with the lack of correlation of the observed directions of accretion driven jets with the orientation of galaxies (Hopkins et al. 2011; King & Pringle 2007). The largest remaining uncertainty in this regard is the competition between accretion onto the central supermassive BH and consumption of gas by star formation as well as the efficiency of stellar and AGN feedback which we have not addressed here. However, measured accretion rates onto the bulge ($200\,{\rm M_\odot}/{\rm yr}$) are largely sufficient to continuously supply gas for a BH accreting at its Eddington limit or above ($\dot{M}_{\rm Edd} = 22\,{\rm M_\odot}/{\rm yr}$ for a $10^9\,{\rm M_\odot}$ BH). Bulges as strongly gravitationally bound as those in our simulation here would, however, ensure that even extreme feedback would have a hard time to revert the continuous inflow of gas. It may indeed take supermassive BHs with several billion solar masses to do this and limit further growth as dis-

cussed by Sijacki et al. (2009) and Di Matteo et al. (2012). We leave a further investigation of these issues to future work.

Note that the picture presented here offers an attractive explanation for the apparent change in the nature of build up of supermassive BHs and galactic bulges with redshift (see Haehnelt & Rees 1993 for some early ideas). At high redshift rare halos are continuously fed (Shankar et al. 2011) with low angular momentum gas streaming in along the filaments penetrating straight to the compact bulge. At intermediate redshift (say $z \sim 2-4$) and probably also in less rare halos at high redshift the gas is fed into the halos with progressively more angular momentum and hangs around more and more in a disc which is intermittently gravitationally unstable. The role of major (and minor) mergers becomes more important but not necessarily dominant. The duty cycle of AGN powered by accretion onto supermassive BHs decreases. At low redshift it becomes harder and harder for the cold filamentary streams to penetrate deep into the halos (Dekel & Birnboim 2006), many especially massive galaxies are now incorporated in galaxy groups and clusters where their direct connection to the the cosmic web is interrupted and this mode of feeding AGNs ceases. The cold gas still present at low redshift now sits preferentially in lower mass halos (see Kauffmann & Heckman 2009 for an extensive discussion of the fueling of AGN at low redshift). The gas in these lower mass halos has high angular momentum which it has to lose by secular processes to reach the central BH. The more massive halos can support a hot atmosphere at low redshift (or have been incorporated into a galaxy group or cluster). Continuous slow accretion of hot gas through cooling flows starts therefore to dominate instead the feeding of the BHs in the massive halos at low redshift (Dubois et al. 2010, 2011).

5   CONCLUSIONS

We have investigated here the formation of a compact central bulge in two rare very massive halos at redshift $z = 6$. Our main results are as follows.

• The typical path for a parcel of fluid entering a halo and eventually ending up in the bulge, is to stream out of a void into the surrounding wall, from there into the filaments defining the intersection of the cosmic walls/sheets, and then along the filaments which penetrate deep into the halo.

• Early on, most of the baryons ending up in the bulge stream nearly radially along the cold filamentary infall directly into a very compact bulge. As time progresses an increasing fraction of the baryons settles first into a compact gravitationally unstable transient central disc from where they progress rapidly into the bulge. By redshift $z = 6$ about half the baryons forming the bulge move first through this surrounding disc before reaching the bulge.

• In the outer part of the halo the angular distribution of the baryonic inflowing matter is stable and reflects the angular distribution of the cosmic web, while well inside the virial radius the angular distribution becomes much more random and changes rapidly.

• A small fraction ($\sim 10\,\%$) of the baryons in the halos falls directly from the structures of the cosmic web into the centre of the halos in the form of proto-galactic clumps; these

clumps are carried along the filamentary streams, that represent more than half of the total accretion of gas, and join the compact central bulge as minor mergers.

• In our simulations most of the baryons in the bulge turn into stars with a remaining gas fraction of 5-30%. The gas fraction is, however, strongly dependent on the resolution and the star formation criterion of the simulation. The gas fraction should also be strongly affected by feedback both from the stars but even more by feedback from the accreting central supermassive BH once the BH has become sufficiently massive. Note again that the simulations used here do not include any feedback.

• The baryon dominated bulge has angular momentum a factor 10-30 lower than the average specific angular momentum of the baryons in the two simulated halos. The baryonic material which is mainly in the form of stars is extremely strongly bound and compact with a peak of the circular velocity approaching 1000 km/s at a radius < 100pc.

• The low value of the angular momentum is due to three effects. First the bulge is preferentially made from material which already has a somewhat lower specific angular momentum than average as it enters the halo along the filaments of the cosmic web. Second the baryonic matter entering the halo from the cosmic environment does so with a broad angular momentum distribution. As the gas streams in cold the lower angular momentum material falls quickly to the centre of the halo due to the lack of pressure support where the randomly oriented angular momentum effectively cancels. Third there is additional angular momentum loss due to dynamical friction on inspiralling proto-galactic clumps, exchange between spin and orbital angular momentum and gravitational instabilities in the disc.

• The fraction of gas streaming nearly radially to the centre of the halo making up the low-angular momentum bulge appears to strongly increase for rare halos. We argue that this is due to the fact that isolated rare halos are connected to the cosmic web more isotropically and with a larger number of filaments. This leads both to lower specific angular momentum when the baryonic matter enters the halo and to more complete angular momentum cancellation when the low angular momentum material streams cold into the compact bulge.

Numerical simulations of galaxy formation are still subject to a range of uncertainties both numerical and in terms of the implemented physics in particularly with respect to feedback due to stars and AGN. The filamentary cold inflow of gas appears nevertheless to emerge as the key ingredient in the formation of the observed compact discs and bulges at high redshift. As we have discussed here it may also be key to the efficient build up of the several billion solar mass black holes inferred to exist as early as $z \sim 6 - 7$.

References

Agertz O., Teyssier R., Moore B., 2009, *MNRAS*, 397, L64
Agertz O., Teyssier R., Moore B., 2011, *MNRAS*, 410, 1391
Alexander D. M., Bauer F. E., Brandt W. N., Hornschemeier A. E., Vignali C., Garmire G. P., Schneider D. P., Chartas G., Gallagher S. C., 2003, *AJ*, 125, 383
Bardeen J. M., Bond J. R., Kaiser N., Szalay A. S., 1986, *ApJ*, 304, 15
Birnboim Y., Dekel A., 2003, *MNRAS*, 345, 349
Bond J. R., Kofman L., Pogosyan D., 1996, *Nature*, 380, 603
Booth C. M., Schaye J., 2009, *MNRAS*, 398, 53
Booth C. M., Schaye J., 2011, *MNRAS*, 413, 1158
Bournaud F., Combes F., Semelin B., 2005, *MNRAS*, 364, L18
Bournaud F., Dekel A., Teyssier R., Cacciato M., Daddi E., Juneau S., Shankar F., 2011, *ApJ Let.*, 741, L33
Bower R. G., Benson A. J., Malbon R., Helly J. C., Frenk C. S., Baugh C. M., Cole S., Lacey C. G., 2006, *MNRAS*, 370, 645
Brooks A. M., Governato F., Quinn T., Brook C. B., Wadsley J., 2009, *ApJ*, 694, 396
Ceverino D., Dekel A., Bournaud F., 2010, *MNRAS*, 404, 2151
Cimatti A., Cassata P., Pozzetti L., Kurk J., Mignoli M., Renzini A., Daddi E., Bolzonella M., Brusa M., Rodighiero G., Dickinson M., Franceschini A., Zamorani G., Berta S., Rosati P., Halliday C., 2008, *A&A*, 482, 21
Codis S., Pichon C., Devriendt J., Slyz A., Pogosyan D., Dubois Y., Sousbie T., 2012, ArXiv e-prints
Croton D. J., Springel V., White S. D. M., De Lucia G., Frenk C. S., Gao L., Jenkins A., Kauffmann G., Navarro J. F., Yoshida N., 2006, *MNRAS*, 365, 11
Daddi E., Alexander D. M., Dickinson M., Gilli R., Renzini A., Elbaz D., Cimatti A., Chary R., Frayer D., Bauer F. E., Brandt W. N., Giavalisco M., Grogin N. A., Huynh M., Kurk J., Mignoli M., Morrison G., Pope A., Ravindranath S., 2007, *ApJ*, 670, 173
Daddi E., Renzini A., Pirzkal N., Cimatti A., Malhotra S., Stiavelli M., Xu C., Pasquali A., Rhoads J. E., Brusa M., di Serego Alighieri S., Ferguson H. C., Koekemoer A. M., Moustakas L. A., Panagia N., Windhorst R. A., 2005, *ApJ*, 626, 680
Danovich M., Dekel A., Hahn O., Teyssier R., 2012, *MNRAS*, p. 2777
Decarli R., Falomo R., Treves A., Labita M., Kotilainen J. K., Scarpa R., 2010, *MNRAS*, 402, 2453
Dekel A., Birnboim Y., 2006, *MNRAS*, 368, 2
Dekel A., Birnboim Y., Engel G., Freundlich J., Goerdt T., Mumcuoglu M., Neistein E., Pichon C., Teyssier R., Zinger E., 2009, *Nature*, 457, 451
Dekel A., Sari R., Ceverino D., 2009, *ApJ*, 703, 785

Di Matteo T., Colberg J., Springel V., Hernquist L., Sijacki D., 2008, *ApJ*, 676, 33

Di Matteo T., Khandai N., DeGraf C., Feng Y., Croft R. A. C., Lopez J., Springel V., 2012, *ApJ Let.*, 745, L29

Di Matteo T., Springel V., Hernquist L., 2005, *Nature*, 433, 604

Dubois Y., Devriendt J., Slyz A., Teyssier R., 2010, *MNRAS*, 409, 985

Dubois Y., Devriendt J., Slyz A., Teyssier R., 2012, *MNRAS*, p. 2188

Dubois Y., Devriendt J., Teyssier R., Slyz A., 2011, *MNRAS*, 417, 1853

Dubois Y., Teyssier R., 2008, *A&A*, 477, 79

Elmegreen B. G., Bournaud F., Elmegreen D. M., 2008, *ApJ*, 688, 67

Fan X., Strauss M. A., Becker R. H., White R. L., Gunn J. E., Knapp G. R., Richards G. T., Schneider D. P., Brinkmann J., Fukugita M., 2006, *AJ*, 132, 117

Górski K. M., Hivon E., Banday A. J., Wandelt B. D., Hansen F. K., Reinecke M., Bartelmann M., 2005, *ApJ*, 622, 759

Haardt F., Madau P., 1996, *ApJ*, 461, 20

Haehnelt M. G., Natarajan P., Rees M. J., 1998, *MNRAS*, 300, 817

Haehnelt M. G., Rees M. J., 1993, *MNRAS*, 263, 168

Haiman Z., 2004, *ApJ*, 613, 36

Häring N., Rix H.-W., 2004, *ApJ Let.*, 604, L89

Heavens A., Peacock J., 1988, *MNRAS*, 232, 339

Hoffman Y., Ribak E., 1991, *ApJ Let.*, 380, L5

Hopkins P. F., Hernquist L., Cox T. J., Di Matteo T., Robertson B., Springel V., 2006, *ApJ Sup.*, 163, 1

Hopkins P. F., Hernquist L., Hayward C. C., Narayanan D., 2011, ArXiv e-prints

Immeli A., Samland M., Gerhard O., Westera P., 2004, *A&A*, 413, 547

Jiang L., Fan X., Bian F., Annis J., Chiu K., Jester S., Lin H., Lupton R. H., Richards G. T., Strauss M. A., Malanushenko V., Malanushenko E., Schneider D. P., 2009, *AJ*, 138, 305

Kauffmann G., Haehnelt M., 2000, *MNRAS*, 311, 576

Kauffmann G., Heckman T. M., 2009, *MNRAS*, 397, 135

Kennicutt Jr. R. C., 1998, *ApJ*, 498, 541

Kereš D., Katz N., Weinberg D. H., Davé R., 2005, *MNRAS*, 363, 2

Kimm T., Devriendt J., Slyz A., Pichon C., Kassin S. A., Dubois Y., 2011, ArXiv e-prints

King A., 2003, *ApJ Let.*, 596, L27

King A. R., Pringle J. E., 2007, *MNRAS*, 377, L25

Knebe A., Power C., 2008, *ApJ*, 678, 621

Komatsu E. et al ., 2011, *ApJ Sup.*, 192, 18

Krumholz M. R., Tan J. C., 2007, *ApJ*, 654, 304

Magorrian J., Tremaine S., Richstone D., Bender R., Bower G., Dressler A., Faber S. M., Gebhardt K., Green R., Grillmair C., Kormendy J., Lauer T., 1998, *AJ*, 115, 2285

Mayer L., Kazantzidis S., Escala A., Callegari S., 2010, *Nature*, 466, 1082

Merloni e., 2010, *ApJ*, 708, 137

Mihos J. C., Hernquist L., 1996, *ApJ*, 464, 641

Mitchell N. L., McCarthy I. G., Bower R. G., Theuns T., Crain R. A., 2009, *MNRAS*, 395, 180

Mortlock D. J., Warren S. J., Venemans B. P., Patel M., Hewett P. C., McMahon R. G., Simpson C., Theuns T., Gonzáles-Solares E. A., Adamson A., Dye S., Hambly N. C., Hirst P., Irwin M. J., Kuiper E., Lawrence A., Röttgering H. J. A.,

2011, *Nature*, 474, 616

Ocvirk P., Pichon C., Teyssier R., 2008, *MNRAS*, 390, 1326

Oser L., Naab T., Ostriker J. P., Johansson P. H., 2012, *ApJ*, 744, 63

Pichon C., Gay C., Pogosyan D., Prunet S., Sousbie T., Colombi S., Slyz A., Devriendt J., 2010, in J.-M. Alimi & A. Fuözfa ed., American Institute of Physics Conference Series Vol. 1241 of American Institute of Physics Conference Series, The Skeleton: Connecting Large Scale Structures to Galaxy Formation. pp 1108–1117

Pichon C., Pogosyan D., Kimm T., Slyz A., Devriendt J., Dubois Y., 2011, *MNRAS*, pp 1739–+

Prunet S., Pichon C., Aubert D., Pogosyan D., Teyssier R., Gottloeber S., 2008, *ApJ Sup.*, 178, 179

Rasera Y., Teyssier R., 2006, *A&A*, 445, 1

Scannapieco C., Wadepuhl M., Parry O. H., Navarro J. F., Jenkins A., Springel V., Teyssier et al. ., 2011, ArXiv e-prints

Shankar F., Weinberg D. H., Miralda-Escude' J., 2011, ArXiv e-prints

Sharma S., Steinmetz M., 2005, *ApJ*, 628, 21

Sijacki D., Springel V., Di Matteo T., Hernquist L., 2007, *MNRAS*, 380, 877

Sijacki D., Springel V., Haehnelt M. G., 2009, *MNRAS*, 400, 100

Silk J., Rees M. J., 1998, *A&A*, 331, L1

Somerville R. S., Hopkins P. F., Cox T. J., Robertson B. E., Hernquist L., 2008, *MNRAS*, 391, 481

Sutherland R. S., Dopita M. A., 1993, *ApJ Sup.*, 88, 253

Teyssier R., 2002, *A&A*, 385, 337

Torrey P., Vogelsberger M., Sijacki D., Springel V., Hernquist L., 2011, ArXiv e-prints

Treister E., Schawinski K., Volonteri M., Natarajan P., Gawiser E., 2011, *Nature*, 474, 356

Tremaine S., Gebhardt K., Bender R., Bower G., Dressler A., Faber S. M., Filippenko A. V., Green R., Grillmair C., Ho L. C., Kormendy J., Lauer T. R., Magorrian J., Pinkney J., Richstone D., 2002, *ApJ*, 574, 740

van den Bosch F. C., Abel T., Croft R. A. C., Hernquist L., White S. D. M., 2002, *ApJ*, 576, 21

van Dokkum P. G., Franx M., Kriek M., Holden B., Illingworth G. D., Magee D., Bouwens R., Marchesini D., Quadri R., Rudnick G., Taylor E. N., Toft S., 2008, *ApJ Let.*, 677, L5

van Dokkum P. G., Kriek M., Franx M., 2009, *Nature*, 460, 717

Wang R., Carilli C. L., Neri R., Riechers D. A., Wagg J., Walter F., Bertoldi F., Menten K. M., Omont A., Cox P., Fan X., 2010, *ApJ*, 714, 699

Whitaker K. E., Kriek M., van Dokkum P. G., Bezanson R., Brammer G., Franx M., Labbé I., 2012, *ApJ*, 745, 179

Willott C. J., 2011, *ApJ Let.*, 742, L8

Willott C. J., McLure R. J., Jarvis M. J., 2003, *ApJ Let.*, 587, L15

APPENDIX A: TRACER PARTICLES TO FOLLOW THE LAGRANGIAN FLOW OF GAS

Tracer particles can be used in Eulerian techniques to follow the Lagrangian path of gas elements. They are passively advected with the gas flow using a simple forward Eulerian
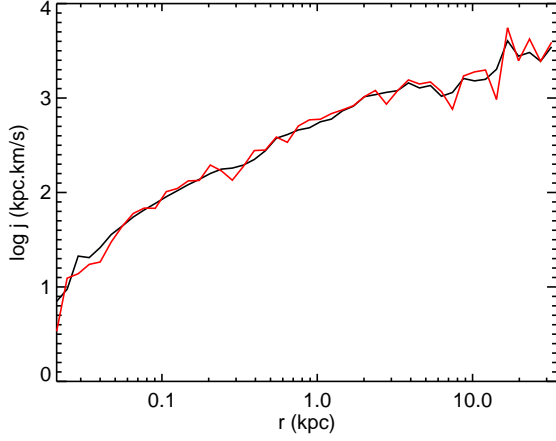
Figure A1. Gas specific angular momentum computed on the actual AMR grid (solid line), or using tracer particles (dashed line) for the SHhr halo at $z = 6$. Profiles are in a very good agreement.

step

$$x_i^{n+1} = x_i + v_i^n \cdot \Delta t^n \,, \tag{A1}$$

using the surrounding gas velocity v_i^n at time t^n from the x_i^n position of the i-th tracer particle. The gas velocity is interpolated using a CIC interpolation scheme on the grid with the size of the cloud equal to the size of host cell. It is a crude, but simple, interpolation of the true gas flow determined by the Euler scheme. More precise (and more complicated) updates of tracer positions could be used (such Runge-Kutta updates) using velocity of the gas at different times. We evaluated the agreement between the gas and tracer particles specific angular momentum profiles in the SHhr simulation at $z = 6$ and find very good agreement between the two (fig. A1).